Electrochemical Chlor-Iron Process for Iron Production from Iron Oxide and Seawater

Berkley B. Noble,[1-2] Louka J. Moutarlier,[1-2] Paul A. Kempler[1-2*]

[1]*Department of Chemistry and Biochemistry, University of Oregon, Eugene, OR 97403*

[2]*Oregon Center for Electrochemistry, University of Oregon, Eugene, OR 97403*

*Correspondence: pkempler@uoregon.edu

Abstract: The iron and steel industry accounts for ~ 8% of global greenhouse gas emissions. Electrochemical reduction of iron ore to metal for electric arc furnaces can enable sustainable steel production, but existing electrochemical processes require expensive capital or electrolytes. We report a low-temperature, electrochemical cell that consumes low-cost and abundant iron oxide and seawater, while co-producing NaOH and Cl_2 with industrially relevant current densities reaching 300 mA cm^{-2} and current efficiencies >90 %. Freestanding films of phase-pure iron were formed after 4 h of continuous, stable electrolysis. The process can lead to levelized costs of iron that are competitive with iron produced in fossil-fuel-powered blast furnaces (< $500 per metric tonne) and the co-produced NaOH can be used for CO_2 mineralization from the air or ocean, creating a net negative-emission process.

Introduction: Ironmaking processes that do not generate greenhouse gas (GHG) emissions are needed for net-zero-emissions energy systems (*1*). Most emissions associated with iron and steel production result from stochiometric quantities of CO_2 (~1.5 kg CO_2 per kg Fe) produced during reduction of iron oxide ores in blast furnaces (*2, 3*). Demand for steel is unlikely to decrease during decarbonization (*4*); immense quantities of iron and steel are needed for manufacturing electric vehicles, buildings with electrified heating/cooling systems (*5*), racking for solar panels, supports for wind turbines, and devices for grid scale energy storage (*6*). Today, steelmaking is responsible for 8% of global GHG emissions, comparable to all passenger vehicles combined (*7*). Recycling of scrap metal can alleviate, but not eliminate, emissions due to metal production, because global demand is predicted to exceed the supply of scrap by about one-third (*8*). Thus, alternate methods of producing iron from ore are needed to ease the carbon emissions burden of the ongoing energy transition (*3, 9*).

Electrochemical cells can support the direct electrification of chemical manufacturing and construction (*9-14*). The electrochemical reduction of iron oxide, using electricity sourced from low-carbon, renewable resources (i.e. wind turbines, solar panels, or hydroelectric dams), and subsequent

1

production of steel in electric arc furnaces, (EAFs), can be used to reduce GHG emission from steelmaking. High-temperature (900–1500 °C) electrochemical processes producing Al (*15, 16*), Mg (*17*), and Fe are known (*18, 19*), and operate at current densities, $J > 5$ A/cm^2. If an iron cathodic process is paired with anodic O$_2$ evolution (e.g. Cr$_{1-x}$Fe$_x$) (*19*), then the electrochemical cell does not produce primary GHG emissions—as opposed to cells using sacrificial carbon anodes, such as in the Hall-Heroult process used to refine aluminum (*16*). The high-temperature and corrosive environment in these processes leads to stringent material requirements and thus increased capital costs of the plant relative to low-temperature cells (*20*). Processes with molten electrolytes are also less tolerant to shutdowns, which may limit their use their capacity to participate in demand response or their ability to directly integrate, "behind-the-meter", with electricity derived from wind and sunlight (*21, 22*).

Grids powered by low-carbon, intermittent resources benefit from flexible electrified manufacturing technologies (*23, 24*). Low-temperature (< 200 °C) electrochemical processes have lower capital costs, which support lower capacity factors in behind-the-meter operation, and offer a greater proportion of flexible load compared to high-temperature processes (*21*). Iron electroplating from sulfate and chloride baths containing ferrous salts at temperatures < 100 °C has been used to refine metal for over 100 y (*25, 26*). Although this process was commercialized for the recovery of iron from waste streams, the dissolution of metal-oxide or metal-sulfide ores consumes stochiometric amounts of acid (e.g. HCl, $153–197/MT in North America in 2022) (*27*), incurring unacceptable operating expenses for commodity production of iron. Direct oxide reduction in alkaline baths at 80–120 °C has been reported (*28*), and electrochemical cells for this reaction yield industrially relevant $J > 1.5$ A cm^{-2} (*29*), while driving an apparent direct reduction of solid Fe$_2$O$_3$ particles to high-purity Fe metal (*30, 31*). In an O$_2$-evolving cell, the anode and cathode reactions are pH-balanced (Fe$_2$O$_3 \rightarrow 2$ Fe $+ \frac{3}{2}$O$_2$) and although the process does not require stochiometric quantities of acid or base for plating, alkaline-soluble silicate impurities from

the ore accumulate in the electrolyte reducing the plating selectivity over time (*28*). Thus direct-oxide

reduction in a pH-balanced cell requires frequent regeneration or purchase of purified alkaline electrolytes.
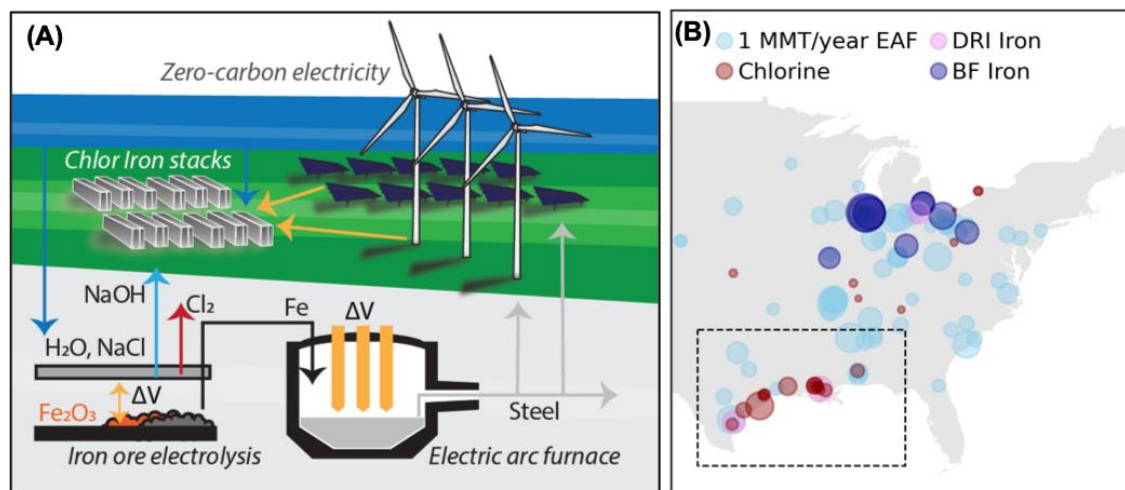

Fig. 1. Integration of the chlor-iron process with low-carbon electricity, Cl₂, and electric arc furnace markets. (A) Iron ore electrolysis, fed by abundant iron oxide, seawater, and zero-carbon electricity, can support further deployment of infrastructure for a net-zero-emissions energy system. **(B)** Co-location of chlorine and electric arc furnaces (EAF) fed by scrap steel and reduced iron provides an opportunity for new chlor-iron plants. Blast furnace (BF) and direct reduced iron (DRI) production are shown for comparison. Circles represent individual production facilities where the diameter is proportional to MMT y^{-1} production. The assumed boundaries for the Gulf Coast region used to compare market size are shown by a dotted line.

Here we report a new electrochemical process yielding high-purity Fe, NaOH(aq), and Cl_2(g), from

abundant and inexpensive iron ore and NaCl(aq) (**Figure 1A**) that directly addresses the economic

challenges related to the purchase of acid/base in previous methods. The co-sale of products from both

the anode and cathode supports a lower breakeven price of Fe (*12, 13*). The anodic reaction yields Cl_2(g)

is valued at \$122–760 MT^{-1} in North America in 2022 (*27*) and is produced at similar scales to reduced

iron in various regions around the globe. For example, the electric arc furnace demand for reduced Fe and

Cl_2 production in the U.S. gulf coast region are ~ 18 MMT y^{-1} and 12 MMT y^{-1}, respectively (**Figure**

1B) (*32, 33*). The co-production of NaOH may assist in purification of metal oxide ores, provide an

additional source of revenue, or be used to stoichiometrically capture and mineralize CO_2 (*34*). Here we

report prototype "chlor-iron" cells designed from electrode materials and membranes available at large manufacturing volumes to enable rapid scale-up to the production of electrolytic iron at the MMT y^{-1} scale. This new cell design yields highly pure Fe metal (98 wt%) at current efficiencies, η_{Fe} >90% while simultaneously producing $Cl_2(g)$ at η_{Cl2} >95% at cell energy efficiency <5 kWh/kg$_{Fe}$.

Results: The new chlor-iron process was developed based on the commercialized membrane chlor-alkali process (**Equation 1**), because the reactors are low-temperature (< 200 °C), deployed at large scale (>5 MMT y^{-1} in the U.S. alone) (*32*), and have accrued decades of profitable operation across the globe.

$$2\ H_2O + 2\ NaCl(aq) \rightarrow H_2(g) + 2\ NaOH(aq) + Cl_2(g) \tag{1}$$

The design replaces H_2 evolution at the cathode with a direct reduction metal-oxide particles to metal (**Equation 2**) and simultaneous produces of Fe(s), NaOH(aq), and $Cl_2(g)$, which are naturally phase separated within the reactor for collection.

$$Fe_2O_3(s) + 3\ H_2O + 6\ NaCl(aq) \rightarrow 2\ Fe(s) + 6\ NaOH(aq) + 3\ Cl_2(g) \tag{2}$$
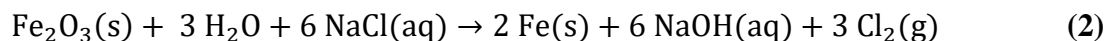
Figure 2A shows a scheme of the cell reactions and **Figure 2B** an image of the batch-reactor prototype. A cation-selective membrane separated the anolyte from catholyte to maintain a steady-state pH gradient while allowing Na^+ to carry the ionic current. The source of Fe was α-Fe_2O_3 aggregate particles, micrometers in diameter composed of primary nanoparticles (**Figure 2D-E),** that were suspended within a strongly basic electrolyte (pH > 14, 7.5 mol/kg NaOH). The metallic cathode product (**Figure 2C,F)** was collected as a solid metal film attached to the current collector. The anode chamber contained an acidified brine (5.7 mol/kg NaCl, pH 2). A thin film of RuO_x, prepared via thermal decomposition of $RuCl_3$ at 400 °C on a Ti current collector, served as the anode catalyst (**Figure 2G, Figure S1**).
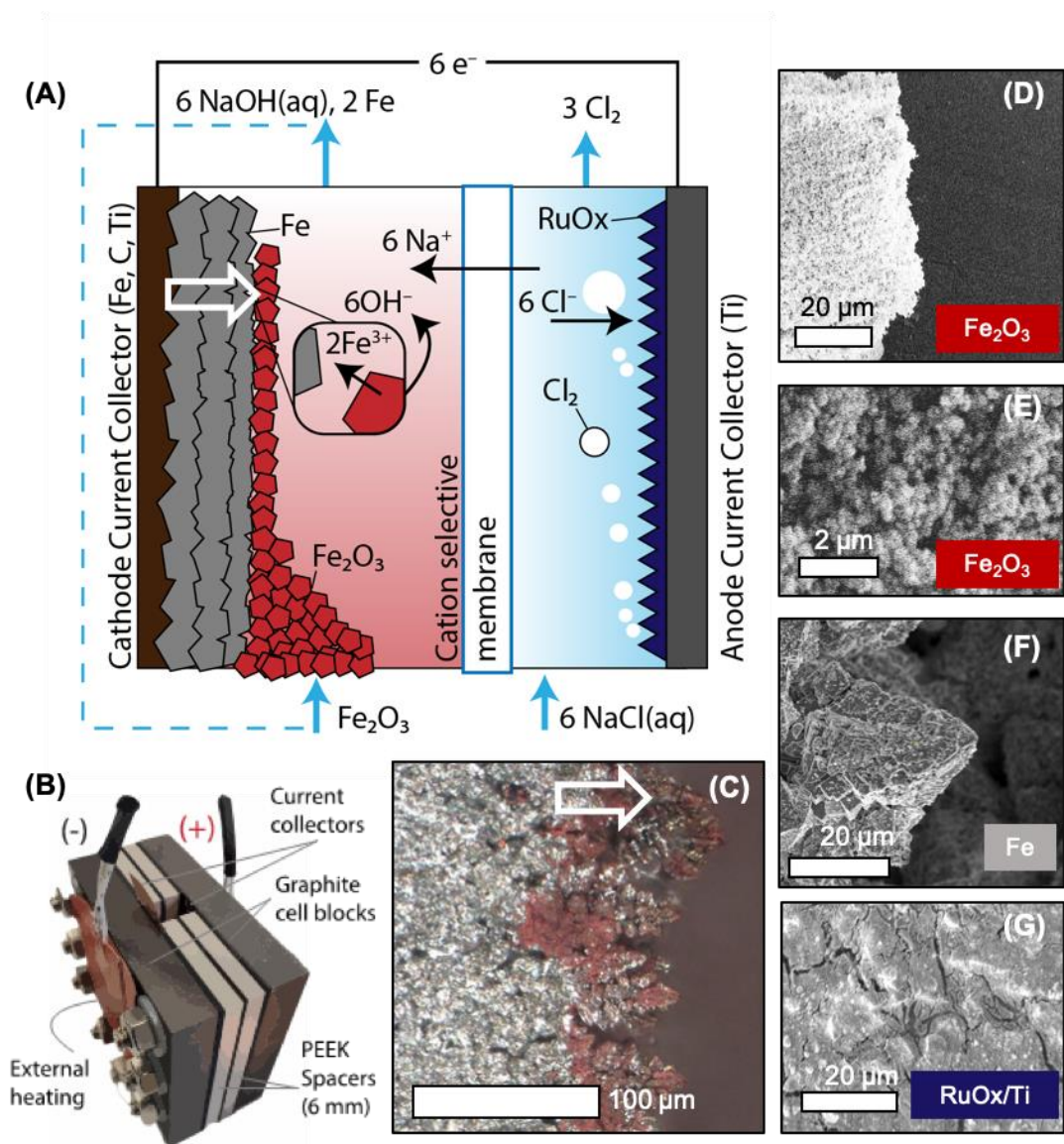
Fig. 2. Summary of the chlor-iron process. (**A**) Fe is reduced from Fe_2O_3 at the cathode, while NaCl is oxidized to $Cl_2(g)$ at the anode, producing NaOH within the cathode compartment. (**B**) Prototype batch cell used in this work. PEEK spacers divide the cell volume, and the cell is heated externally through graphite end plates. (**C**) Optical microscope image of Fe cross section showing adsorbed Fe_2O_3 on the growth surface. The growth direction is indicated by the white arrow. (**D**) SEM image of Fe_2O_3 agglomerate particle consisting of (**E**) nanoscale primary particles. (**F**) SEM image of Fe plated at 100 mA cm^{-2}. (**G**) Representative, as-deposited RuO_x surface that served as the anodic electrocatalyst.
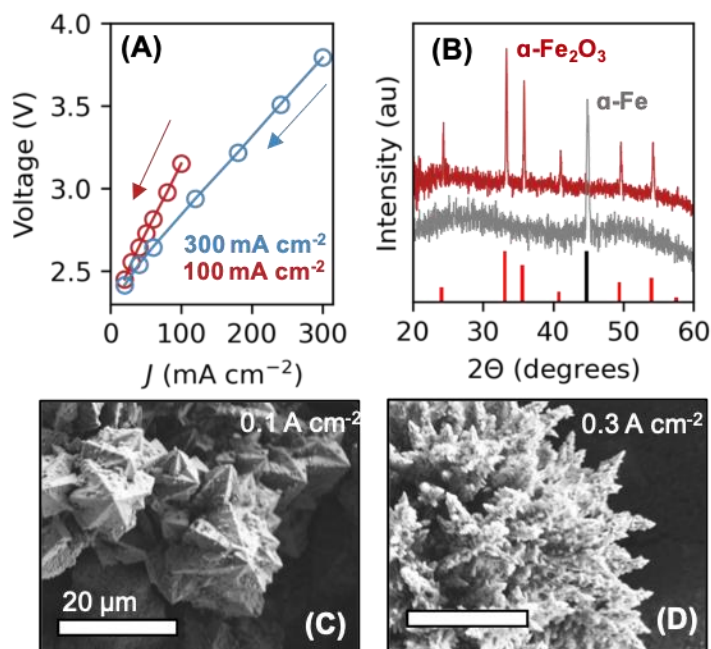
Fig. 3. Operating characteristics of the batch chlor-iron cell. (**A**) Current-voltage behavior of the batch chlor-iron cell charged with 25 wt% α-Fe$_2$O$_3$, 7.5 mol/kg NaOH(aq) in the catholyte and 6 mol/kg NaCl in the anolyte separated by a Nafion 115 membrane and externally heated to 80 °C. The polarization curve was recorded after a 30 min break-in period representing steady-state operation of the cell. (**B**) Powder X-ray diffraction of reagent α-Fe$_2$O$_3$ (dark red) and the reduced Fe product (gray) after 30 min of electrolysis at 100 mA cm^{-2}. Simulated diffraction peaks for α-Fe$_2$O$_3$ and α-Fe are represented in red and black (**C**) Scanning electron micrograph of Fe surface after 30 min of electrolysis at 100 mA cm^{-2} and (**D**) 300 mA cm^{-2}, both inset scale bars represent 20 µm.

Figure 3A shows the polarization behavior of the chlor-iron process after two separate 30 min electrolysis experiments at 100 and 300 mA cm^{-2} (**Figure 3A**, **Figure S2**). The onset of the Faradaic efficiency towards Fe, η_{Fe} was evaluated based on the mass of Fe collected from the current collector. The product purity and phase composition Fe films were analyzed using X-ray diffraction (XRD), electron probe microanalysis (EPMA), and energy-dispersive X-ray analysis (EDX). The Fe content in the film as measured by EPMA, 96.8(6)%, and (EDX), 98.3(7)%, was consistent with films composed primarily of metallic Fe with a small amount of oxide present either on the film surface (**Figure S4**) or as inclusions within the film. XRD patterns (**Figure 3B**) of the reactant powder (red) were compared to a crushed

6

product film after the top layer was scraped from the surface (grey) showing only the presence of α-Fe$_2$O$_3$ in the reactant while the metallic product exhibited a single peak assigned to α-Fe(110).
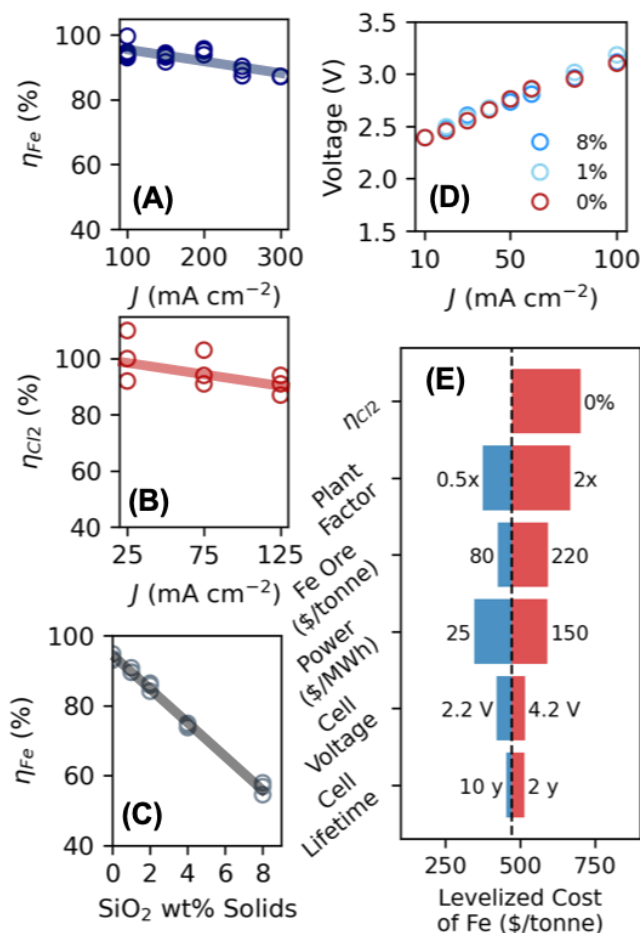

Fig. 4. Process parameters and sensitivities of the batch chlor-iron cell. (**A**) Relationship between η_{Fe} and J for Fe plated in a batch cell divided by Nafion 115. η_{Fe} >85 % was sustained for current densities 100–300 mA cm^{-2}. (**B**) Relationship between η_{Cl2} and J for RuO$_x$ anodes, evaluated in a batch cell with 5.7 mol kg^{-1} NaCl (pH = 2) in both the anolyte and catholyte divided by Nafion 115. (**C**) Relationship between η_{Fe} and SiO$_2$ content in a representative ore mixture containing 0–8 wt% SiO$_2$ with the remainder Fe$_2$O$_3$ (the total amount of solids fed to the reactor was kept constant at 25 wt%). η_{Fe} was measured in an identical cell to (**A**) with the J = 100 mA cm^{-2}. (**D**) Polarization behavior of the batch cell in the presence of SiO$_2$ at 0 wt%, 1 wt%, and 8 wt% (solids basis). (**E**) Sensitivity of the levelized cost of iron relative to six critical model parameters. The base case is described in the **Supplementary Materials**.

The morphology of reduced Fe was dependent on J. Films deposited at 100 mA cm^{-2} were largely free of pinholes with limited branching within the film microstructure. Secondary particles of Fe within the film structure were generally tens of micrometers in diameter (**Figure 3C**). The morphology of films

7

produced at 300 mA cm^{-2} contained a surface base layer with multiple 30 μm diameter pinholes (**Figure S3**) that extended to the current collector surface.

The hydrogen evolution reaction and oxygen evolution reaction compete with the cathodic and anodic reactions in the chlor-iron cell, respectively, and so the selectivity towards the desired Fe and Cl$_2$ products at the RuO$_x$ surface as a function of J was investigated (*35*). The selectivity towards iron plating, η_{Fe}, was >94 % for $J \leq 200$ mA cm^{-2} (**Figure 4A)** and η_{Fe} decreased to 87% at 300 mA cm^{-2}. Further increases to J produced excess H$_2$(g), such that gassing prevented reliable cell-voltage measurements within the batch cell, and thus η_{Fe} was not quantified at $J > 300$ mA cm^{-2}. For the batch cell, the selectivity towards Cl$_2$(g) evolution was evaluated in a cell containing 5.7 mol/kg NaCl (pH = 2) in both the anolyte and catholyte, with $\eta_{Cl2} = 91(3)\%$ at $J = 125$ mA cm^{-2}.

The use of lower-purity Fe oxides as reagents was investigated to assess the reaction scope. A representative commercial-grade red iron-oxide powder, which contained significant quantities of Si (8 w%t), Al (4 wt%), or Mg (2 wt%) (**Table S1**), was electrolyzed at $J = 100$ mA cm^{-2} but led to $\eta_{Fe} < 30\%$. Next, SiO$_2$ and Al$_2$O$_3$ particles were blended with purified α-Fe$_2$O$_3$ as feedstocks for the chlor-iron cell. At $J = 100$ mA cm^{-2}, η_{Fe} was inversely proportional to the quantity of SiO$_2$ fed to the cell (**Figure 4C**), although the polarization behavior was largely unaffected by SiO$_2$. At an increased J of 300 mA cm^{-2}, 8 wt% SiO$_2$ in the catholyte led to an $\eta_{Fe} < 37\%$ during electrolysis (**Table S2**). The addition of Al$_2$O$_3$ at 4 wt% did not significantly impact η_{Fe} at either J.

An electrochemical flow cell that maintained constant electrolyte volumes and concentrations was prepared for longer duration evaluation of the chlor-iron process and also enabled continuous collection of Cl$_2$(g) for measurement of η_{Cl2} prior to quenching (**Figure 5A**). Expelled electrolyte due to gas evolution in the cathode chamber was collected and stored, while Cl$_2$(g) was quenched in either a methyl-

orange indicator solution used to measure η_{Cl2} via endpoint detection (*36*), or an alkaline solution that rapidly converted $Cl_2(g)$ to soluble $HClO/ClO^-$ (**Figure S6**).
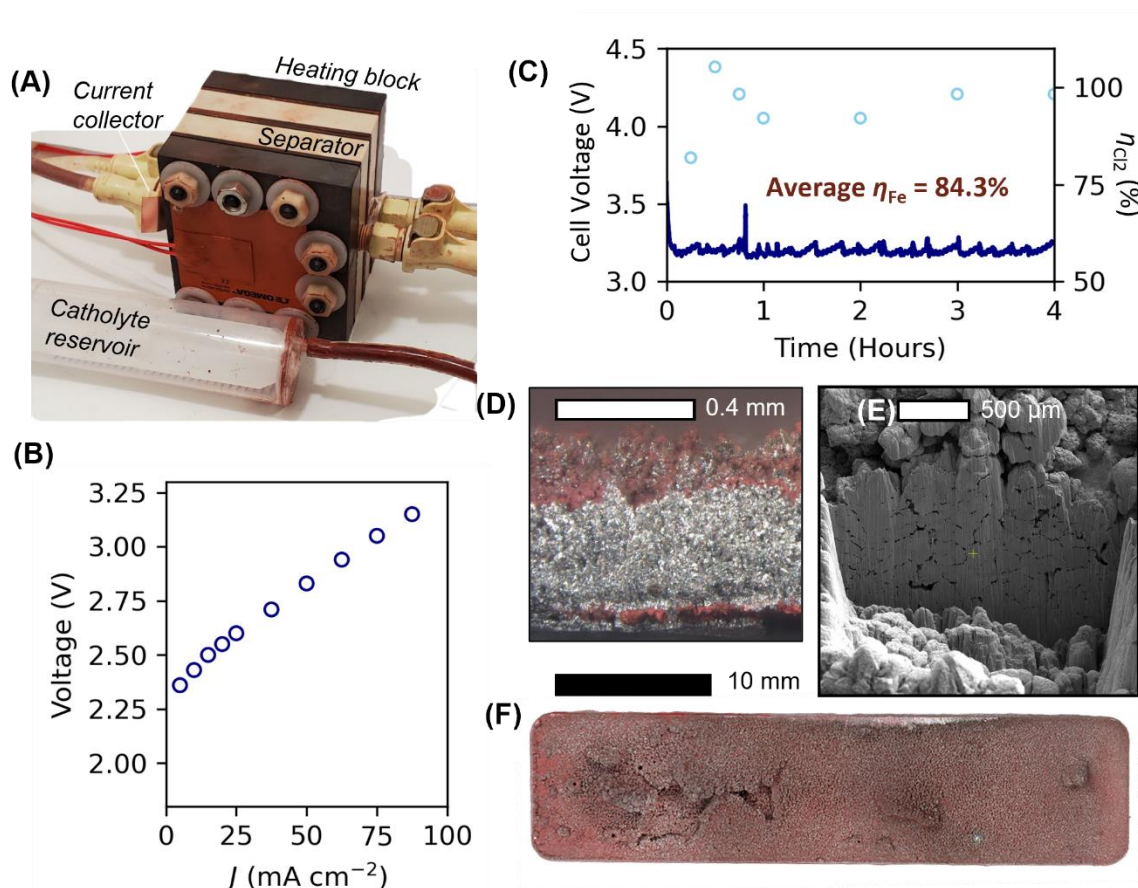

Figure 5: Continuous flow operation of the chlor-iron process (**A**) Flow cell used for extended testing of the chlor-iron process. The direction of flow within the cell was aligned vertically with respect to gravity during operation with electrolyte pumped in through the base of the cell. (**B**) Steady-state polarization behavior of the chlor-iron cell. (**C**) Cell voltage vs. time for a constant-current electrolysis at 100 mA cm^{-2} for 4 h with periodic measurements of η_{Cl2} and an average η_{Fe} assessed at the end of electrolysis. Cleaved cross-section (**D**), top-down image (**F**), and focused-ion-beam cross section (**E**) of the film produced in (**C**).

A bilayer membrane designed for the chlor-alkali process (N2030, Chemours) maintained an acidic pH environment at the anolyte, whereas the anolyte pH rapidly increased to >10 in cells prepared with Nafion 115 membranes or porous diaphragms. Both the N2030 and Nafion 115 membranes led to cells with similar polarization responses, whereas a porous diaphragm separator led to substantially lower cell voltages (**Figure S7**). The cell voltage was consistent at ~3.2 V throughout a 4 h constant current hold

at 100 mA cm^{-2}, whereas the measured η_{Cl2} ranged from 82–105% during the first 20 min of reaction before stabilizing at 95(3)% from hours 1–4 and the average η_{Fe} was 84%. The polarization behavior of the cell after testing was similar to the polarization behavior measured after 30 min (**Figure S5**). The Fe films produced in multi-hour reactions were easily detached from the current collector surface as a free-standing film (**Figures 5D and 5E**). SEM and optical microscopy revealed the films to mostly consist of dense Fe metal particles, having diameters ~10–50 µm with a sparse population of voids having diameters < 10 µm (**Figure 5D**). The thickness of the film was mostly uniform, with the exception of small clumps that formed within the slurry.

Discussion: Fe and Cl$_2$(g) were produced at $J = 100$ mA cm^{-2} and $\eta > 90\%$ such that the coupling of the anodic and cathodic reactions did not preclude independent production and collection of Fe and Cl$_2$ (**Figure 2**, **Figure 5**, **Supplementary Materials**). The micron-scale morphology, η_{Fe}, and purity of the Fe deposits in this work are consistent with previous reports of Fe films produced in undivided alkaline cells evolving O$_2$(g) (*28, 30, 37*). Cells separated by a conventional cation-exchange membrane (**Figure 4A**), a porous diaphragm (**Figure S7**), and a specialty bilayer cation exchange membrane (**Figure 5**) all yielded $\eta_{Fe} > 90\%$, consistent with prior reports on undivided cells in concentrated NaOH (*28, 29, 38*), indicating that Cl$^-$ crossover through the cation-selective membrane was marginal or else had a marginal effect on the Fe-plating reaction. The chlorine evolution reaction was most significantly affected by the anolyte pH, and the use of a specialty bilayer membrane (N2030) was required to prevent crossover of the 7.5 mol/kg NaOH in the catholyte through the membrane to the dilute acid in the anolyte. The large pH gradient between the anolyte and catholyte led to an increase in the operating cell voltage (>3 V) relative to a cell producing only Fe and O$_2$ from a single, alkaline electrolyte (1.7 V) (*28, 38*). While the voltages observed are comparable to those used in chlor-alkali cells, the maximum J explored in this work is about 50% of the operating current in state-of-the-art chlor-alkali cells ($J > 600$ mA cm^{-2}). To enable increases to J at

similar cell voltages, future work should study the role of reactant oxide phase and particle diameter (*39*), the influence of cathode morphology on polarizability, and improved gas release from the anode and cathode to minimize cell resistance (*40*) (**Figure 3A**).

A technoeconomic analysis of the levelized cost of electrolytic iron assumed plants constructed at a similar capital cost to existing chlor-alkali plants (**Figure 4E**) (*20, 41*). We justify this assumption based on the similar operating conditions and bill of materials of the chlor-iron and chlor-alkali processes. The operating voltages and η_{Cl2} obtained in the 4 cm^2 cell were used for the base case (**Figure 5B**) and we have also reported the sensitivity of the cost of iron to changes in η, the capital cost of the plant, the cost of iron ore, the cost of electric power, the cell voltage, and the cell lifetime. For industrial electricity prices ~\$75/MWh, the levelized cost of iron is most sensitive to the capital cost of the plant and η, but is relatively insensitive to the cell voltage and replacement schedule. This finding suggests that increased electricity costs due to increased cell voltage, provided that they enable effective stack costs (on a \$ MT^{-1} capacity basis) that are comparable to industrial chlor-alkali cells, are preferable to reach minimum costs for iron production. Both η_{Fe} and η_{Cl2} are sensitive to cell operating conditions (**Figure 4 A–C**) and new additives may be required to enable increased throughput without commensurate tradeoffs in product selectivity.

The presence of SiO_2 within the catholyte did not appear to influence the polarization behavior of the cell (**Figure 4D**) and was not incorporated into the film but led to a substantially reduced η_{Fe} (**Figure 4C**). Whereas molten oxide electrolyzers operate with high selectivity in electrolytes containing SiO_2, Al_2O_3, and MgO, low temperature electrolyzers should first remove SiO_2 from low-purity iron oxide ores to < 2 wt% in order to yield catholyte conditions that enable $\eta_{Fe} > 90\%$ (**Figure 4C**). Ores of similar purity (SiO_2 and $Al_2O_3 < 5$ wt%) are required for Directly Reduced Iron processes, to avoid sticking in the fluidized bed and excess slag formation (*42*). Nevertheless, the chlor-iron process may be tolerant to

lower-grade ores if co-product NaOH is used to pre-leach aluminates and silicate, which are soluble in concentrated alkali solutions, from the feed.

Although a Ti-supported RuO_x anode was used in this work, we expect commercialized anodes to yield similar efficiencies and improved durabilities to their intended application in the chlor-alkali process (43), in the absence of significant crossover of OH^- or dissolved metal oxides. The anodic electrocatalyst films, current collectors, and membranes used in the chlor-iron electrochemical cells reported herein are available as part of an existing large-volume supply chain supporting the chlor-alkali industry. Moreover, the liquid electrolytes fed to the anode and cathode compartments are compatible with the chlor-alkali process, such that this method of ironmaking could be scaled along a parallel manufacturing process or even as a retrofit of existing systems. Although production and offtake vary based on location, we have identified regions where the capacities are well matched and available at the >10 MMT y^{-1} scale, supporting potential of this process to substantially impact ironmaking emissions (**Figure 1B**).

The generation of OH^- at the cathode that is not consumed at the anode led to a process that is a net-producer of NaOH as opposed to a net-consumer of NaOH, HCl, or H_2SO_4, which must be leveraged against the final breakeven cost of the Fe. Separation costs associated with Fe and $Cl_2(g)$ are expected to be marginal, whereas significant separations may be necessary to remove metal/metal-oxide impurities from the NaOH produced in the catholyte. Low-purity NaOH could either be used as a purifying reagent for commercial-grade iron ore, or even used to capture and mineralize CO_2, leading to a net-negative process for ironmaking thereby offsetting downstream emissions associated with steelmaking (34). Assuming the chlor-iron process is capped by the global market for $Cl_2(g)$ (~100 MMT y^{-1}), the production of 53 MMT y^{-1} decarbonized Fe and 115 MMT y^{-1} low purity NaOH could potentially avoid 115 MMT y^{-1} of CO_2 emissions associated with the blast furnace/basic oxygen furnace process and additionally capture 126 MMT y^{-1} CO_2 for mineralization (**Supplementary Materials**). Chlor-iron cells producing

12

excess NaOH could potentially provide inexpensive streams of electrolyte to alkaline electrolyzers producing Fe and O_2 to satisfy the remaining demand for primary Fe production (**Supplementary Materials**).

The optimal morphology, purity, and throughput required for Fe deposition likely depend on the use case of the Fe films. The morphology (particle diameter ~10-50 µm) and purity (>95%) of the Fe produced is consistent with direct-reduced iron sponge used as a feedstock for electric arc furnaces (**Figure 2B**, **Figure S8**) (*8*). This method could also be used to produce high surface area, monolithic iron electrodes for use in aqueous metal-air batteries (*6, 44-46*). Understanding the use of cations and sulfide additives for suppressing hydrogen evolution during the plating process, and the influence of *J* on the film morphology, are useful future studies (*47, 48*).

In summary, a new electrochemical cell based on materials used in the membrane chlor-alkali process yielded a scalable, efficient (<5 MWh MT_{Fe}^{-1}), and high-throughput (>100 mA cm^{-2}) process for ironmaking that would produce zero or even net-negative direct GHG emissions (**Figure S5**). The overall cell reaction requires only low-cost iron oxide and seawater/brine as reactants. Fe was produced as easily collected free-standing films with >95 wt% purity, suitable for use in electric arc furnaces, and Cl_2 was collected at industrially-relevant rates and selectivity. The co-production of NaOH is a distinguishing feature of this approach to ironmaking and could be used to purify low-grade iron ore to remove silicates or potentially used in a downstream process for CO_2 capture and mineralization, leading to a net-negative GHG emission ironmaking process with the potential to avoid/capture 240 MMT_{CO2} y^{-1}.

Materials and Methods

Electrochemical Cell and Characterization

The electrochemical cell was prepared from two graphite plates supporting a polished Cu foil cathode, a Ti/RuO$_x$ anode, neoprene rubber gaskets, polyether ether ketone (PEEK) plates, and a cation-

exchange membrane. The anode and cathode compartments were defined by 6 mm thick polyether ether ketone (PEEK) spacers and were separated by a cation-selective membrane; Nafion 115 or GI-N417 were used as membranes in the batch cell, whereas a specialty bilayer membrane (N2030), designed to prevent hydroxide crossover in commercial chlor-alkali cells was used to separate the compartments of the flow cell. All cells were externally heated to 80 °C through a silicone heating mat (Omega Engineering) fixed to graphite endplates in contact with the current collectors. A thermocouple was inserted into the graphite plate to measure the cell temperature and give feedback to a simple controller providing power to the heating pads.

Current was supplied to the cell from a programmable DC power supply and voltage was recorded using a Biologic SP200 potentiostat. The standard catholyte was an alkaline suspension of 25 wt% α-Fe_2O_3 mixed with 7.5 mol/kg NaOH(aq) and the anolyte was 5.7 mol/kg NaCl(aq) adjusted to pH = 2 using 1 M HCl(aq).   The effects of impurities were measured with a 25 wt% suspension of SiO_2/Al_2O_3/Fe_2O_3 in 7.5 mol/kg NaOH(aq), where the mass fraction of SiO_2 or Al_2O_3 was expressed relative to the mass of the solids prior to addition to the basic catholyte.

Cl_2 production and detection

The production of Cl_2(g) was quantified using an indicator solution containing methyl orange. Cl_2 is a reactive and toxic gas that should not be allowed to accumulate without redundant safety controls. Cl_2(g) produced in these studies was immediately reacted with titrant or quenched in a chilled, alkaline bath prior to disposal.

References:

1.   S. J. Davis *et al.*, Net-zero emissions energy systems. *Science* **360**, eaas9793 (2018).
2.   Z. Fan, S. J. Friedmann, Low-carbon production of iron and steel: Technology options, economic assessment, and policy. *Joule* **5**, 829-862 (2021).
3.   V. Vogl, O. Olsson, B. Nykvist, Phasing out the blast furnace to meet global climate targets. *Joule* **5**, 2646-2662 (2021).

4. S. Wang *et al.*, Future demand for electricity generation materials under different climate mitigation scenarios. *Joule*, (2023).

5. J. Rosenow, D. Gibb, T. Nowak, R. Lowes, Heating up the global heat pump market. *Nature Energy* **7**, 901-904 (2022).

6. W. H. Woodford, S. Burger, M. Ferrara, Y.-M. Chiang, The iron-energy nexus: A new paradigm for long-duration energy storage at scale and clean steelmaking. *One Earth* **5**, 212-215 (2022).

7. IEA, "*Iron and Steel Technology Roadmap*," (Paris, 2020).

8. D. Raabe, C. C. Tasan, E. A. Olivetti, Strategies for improving the sustainability of structural metals. *Nature* **575**, 64-74 (2019).

9. P. Fennell, J. Driver, C. Bataille, S. J. Davis, Cement and steel—nine steps to net zero. *Nature* **603**, 574-577 (2022).

10. Z. J. Schiffer, K. Manthiram, Electrification and decarbonization of the chemical industry. *Joule* **1**, 10-14 (2017).

11. L. D. Ellis, A. F. Badel, M. L. Chiang, R. J.-Y. Park, Y.-M. Chiang, Toward electrochemical synthesis of cement—An electrolyzer-based process for decarbonating CaCO3 while producing useful gas streams. *PNAS* **117**, 12584-12591 (2020).

12. F. W. Lucas *et al.*, Electrochemical routes for the valorization of biomass-derived feedstocks: from chemistry to application. *ACS Energy Lett.* **6**, 1205-1270 (2021).

13. C. E. Finke *et al.*, Economically advantageous pathways for reducing greenhouse gas emissions from industrial hydrogen under common, current economic conditions. *Energy Environ. Sci.* **14**, 1517-1529 (2021).

14. N. Downes *et al.*, Si Electrochemical Liquid Phase Epitaxy: Low-Temperature Growth of Hyperdoped Epitaxial Si Films. *Chem Mater.*, (2022).

15. D. R. Sadoway, Inert anodes for the Hall-Heroult cell: the ultimate materials challenge. *Jom* **53**, 34-35 (2001).

16. W. E. Haupin. Electrochemistry of the Hall-Heroult process for aluminum smelting. *J. Chem Educ.* **60**, 279 (1983).

17. Y. Castrillejo, A. Martinez, R. Pardo, G. Haarberg, Electrochemical behaviour of magnesium ions in the equimolar $CaCl_2$ NaCl mixture at 550° C. *Electrochim. Acta* **42**, 1869-1876 (1997).

18. H. Kim, J. Paramore, A. Allanore, D. R. Sadoway, Electrolysis of molten iron oxide with an iridium anode: the role of electrolyte basicity. *J. Electrochem. Soc.* **158**, E101 (2011).

19. A. Allanore, L. Yin, D. R. Sadoway, A new anode material for oxygen evolution in molten oxide electrolysis. *Nature* **497**, 353-356 (2013).

20. C. Stinn, A. Allanore, Estimating the capital costs of electrowinning processes. *Electrochem. Soc. Interface* **29**, 44 (2020).

21. T. Müller, D. Möst, Demand response potential: available when needed? *Energy Policy* **115**, 181-198 (2018).

22. C. Hoffmann *et al.*, Assessing the realizable flexibility potential of electrochemical processes. *Ind. Eng. Chem. Res.* **60**, 13637-13660 (2021).

23. T. H. Ruggles, J. A. Dowling, N. S. Lewis, K. Caldeira, Opportunities for flexible electricity loads such as hydrogen production from curtailed generation. *Adv. Appl. Energy* **3**, 100051 (2021).

24. J. D. Jenkins, M. Luke, S. Thernstrom, Getting to zero carbon emissions in the electric power sector. *Joule* **2**, 2498-2510 (2018).

25. A. S. Ramage. (1911), US1007388A.

26. A. Boucher. (1914), US1086132A.

27. "Chemical Price Trends" (ChemAnalyst, 2022) [No author]

28. J. A. M. Leduc, R. E. Loftfield, L. E. Vaaler, Electrolytic Iron Powder from a Caustic Soda Solution. *J. Electrochem. Soc.* **106**, 659 (1959).

29. B. Yuan, O. E. Kongstein, G. M. Haarberg, Electrowinning of Iron in Aqueous Alkaline Solution Using a Rotating Cathode. *J. Electrochem. Soc.* **156**, D64 (2009).

30. A. Allanore, H. Lavelaine, G. Valentin, J. Birat, F. Lapicque, Iron metal production by bulk electrolysis of iron ore particles in aqueous media. *J. Electrochem. Soc.* **155**, E125 (2008).

31. A. Allanore *et al.*, Observation and modeling of the reduction of hematite particles to metal in alkaline solution by electrolysis. *Electrochim. Acta* **55**, 4007-4013 (2010).

32. "Chlorine & Building Materials Project: Phase 1 Africa, The Americas, and Europe," (Healthy Building Network, 2018).

33. "Global Steel Plant Tracker. (Global Energy Monitor, 2022).

34. D. W. Keith, G. Holmes, D. S. Angelo, K. Heidel, A process for capturing CO2 from the atmosphere. *Joule* **2**, 1573-1594 (2018).

35. P. Adiga *et al.*, Breaking OER and CER scaling relations via strain and its relaxation in RuO2 (101). *Mater. Today Energy* **28**, 101087 (2022).

36. D. Wintrich *et al.*, Enhancing the selectivity between oxygen and chlorine towards chlorine during the anodic chlorine evolution reaction on a dimensionally stable anode. *ChemElectroChem* **6**, 3108-3112 (2019).

37. G. M. Haarberg, B. Yuan, Direct electrochemical reduction of hematite pellets in alkaline solutions. *ECS Trans.* **58**, 19 (2014).

38. A. Allanore, H. Lavelaine, J. P. Birat, G. Valentin, F. Lapicque, Experimental investigation of cell design for the electrolysis of iron oxide suspensions in alkaline electrolyte. *J. Appl. Electrochem.* **40**, 1957-1966 (2010).

39. A. Navrotsky, L. Mazeina, J. Majzlan, Size-driven structural and thermodynamic complexity in iron oxides. *Science* **319**, 1635-1638 (2008).

40. P. A. Kempler, R. H. Coridan, N. S. Lewis, Effects of bubbles on the electrochemical behavior of hydrogen-evolving Si microwire arrays oriented against gravity. *Energy Environ. Sci* **13**, 1808-1817 (2020).

41. C. A. Manfield, B. M. Depro, "Economic Analysis of Air Pollution Regulations: Chlorine Industry," (2000).

42. M. Small, Direct reduction of iron ORE. *JOM* **33**, 67-75 (1981).

43. S. Trasatti, Electrocatalysis: understanding the success of DSA®. *Electrochim. Acta* **45**, 2377-2385 (2000).

44. B. T. Hang *et al.*, The effect of additives on the electrochemical properties of Fe/C composite for Fe/air battery anode. *J. Power sources* **155**, 461-469 (2006).

45. A. K. Manohar *et al.*, A High-Performance Rechargeable Iron Electrode for Large-Scale Battery-Based Energy Storage. *Journal of The Electrochemical Society* **159**, A1209-A1214 (2012).

46. J. F. Parker *et al.*, Rechargeable nickel–3D zinc batteries: An energy-dense, safer alternative to lithium-ion. *Science* **356**, 415-418 (2017).

47. D. Mitra, A. S. Rajan, A. Irshad, S. R. Narayanan, High Performance Iron Electrodes with Metal Sulfide Additives. *J. Electrochem. Soc.* **168**, 030518 (2021).

48. M. C. O. Monteiro, A. Goyal, P. Moerland, M. T. M. Koper, Understanding Cation Trends for Hydrogen Evolution on Platinum and Gold Electrodes in Alkaline Media. *ACS Catal.* **11**, 14328-14335 (2021).

Authors contributions: Conceptualization, PAK**;** Methodology, BBN and PAK**;** Investigation, BBN, LJM, and PAK**;** Visualization, PAK and BBN**;** Writing – Original Draft, BBN**;** Writing – Review and Editing, BBN, LJM, and PAK**;** Supervision, PAK**;** Funding Acquisition, PAK

Competing interests: PAK has filed a provisional patent (No. 63/349,953) on the chlor-iron process.

Data and materials availability: All data are available in the manuscript or the supplementary materials.

Supplementary Materials
Electrochemical Chlor-Iron Process for Iron Production from Iron Oxide and Seawater

Berkley B. Noble,[1-2] Louka J. Moutarlier,[1-2] Paul A. Kempler[1-2*]

[1]*Department of Chemistry and Biochemistry, University of Oregon, Eugene, OR 97403*
[2]*Oregon Center for Electrochemistry, University of Oregon, Eugene, OR 97403*
*Correspondence: pkempler@uoregon.edu

Supplementary Materials and Methods

Materials

α-Fe$_2$O$_3$ (98% purity, metals basis), NaOH (Extra Pure, 50.0 wt% aq), Al$_2$O$_3$ (99.7%, <0.04% SiO$_2$), MgO (98%), and anhydrous RuCl$_3$ (47.7% min), were purchased from Thermo Scientific whereas HCl (ACS Grade), and NaCl (ACS Grade) were purchased from Fisher Scientific. SiO$_2$ was purchased from U.S. Nano. Nafion 115 and GI-N417 membranes were purchased from Fuel Cell Store, Zirfon® UTP-500 was provided by Agfa, and N2030 was provided by Chemours. Ti foil (99.99%) was purchased from Futiantian Technology Co. and Cu foil (99.99%) from MTI Corporation. A representative "commercial-grade" iron oxide powder was purchased from Alpha Chemical. KBr was sourced from J.T. Baker and Methyl Orange (97%) from Aldrich. All solutions were prepared using water from a Millipore deionized water system having a resistivity >18.1 MΩ.

Anode preparation

Ti-supported RuO$_x$ served as Cl$_2$ evolving anodes and were prepared following the method of Trasatti.[1] Briefly, 80 mg of RuCl$_3$ was dissolved in 20 mL of 20 wt% HCl(aq) and then heated to evaporate excess liquid, yielding a dark residue, free of visible particles. This residue was resuspended in 5 mL of isopropyl alcohol to form a Ru(III) ink and stored in the dark at room temperature until use. Ti foils were soaked in 20 wt% HCl(aq) for 10 min and then repeatedly brush-coated with the Ru(III) ink, dried on a hot plate at 150 °C, and suspended in stagnant air within an upright furnace at 400 °C for 10 min. The coating, drying, and oxidation process was repeated until the catalyst loading was ~2 mg/cm^2.

Optimization of Cathode Conditions

A batch cell separated by Nafion 115 (Chemours) was used to determine the optimal current density conditions for Fe plating. At $J <$ 100 mA cm^{-2}, a Biologic SP300 potentiostat supplied the current and recorded voltage. For $J >$ 100 mA cm^{-2}, a 30V-10A benchtop power supply provided the provided current and a Biologic SP300 recorded voltage. The temperature of the cell was monitored with a negative

temperature coefficient thermistor and controlled using a voltage relay connected to silicone heating mats integrated with the cell. The plating efficiency was determined from the weight of the washed and dried cathode post-plating, as the composition of Fe by mass was consistently in excess of 95%.

Impurity Testing

The source of Fe used for the catholyte suspension impacted the performance of the cell. A high purity source of Fe_2O_3 (Thermo Scientific) was used as the base line and led to a substantially increased faradaic efficiency towards Fe in comparison to a lower purity red iron oxide powder (Alpha Chemicals). The effect of metal oxide impurities on Fe electrolysis was studied using a factorial experiment with a single replicate and a randomized run order that screened for primary and cross effects of SiO_2, Al_2O_3, and J. The maximum concentration of metal oxide was selected based on the concentrations present in the "commercial grade" ore (8 wt% SiO_2 and 4 wt% Al_2O_3), which was found to lead to low (~15%) current efficiency towards Fe. Further investigation of SiO_2 contamination was conducted after it was identified as a critical parameter influencing η_{Fe}. Despite the direct, inverse relationship between the SiO_2 content in the electrolyte and the plating efficiency of Fe, Si was not detected in the films using EPMA.

Symmetric cell for anode evaluation

A mirrored cell with NaCl acid solution on both sides of the Nafion membrane was used to evaluate the dependence of η_{Cl2} on J. For safety, $Cl_2(g)$ leaving in the anode effluent was immediately quenched in >10 wt% NaOH. After the anode gas production cleared the effluent tube, the tube was rinsed with DI water and then submerged in the methyl orange solution to quantify $Cl_2(g)$ production via endpoint detection.

Quantifying chlorine production.

Chlorine produced in a flow cell separated by N2030 (Chemours) was quantified using endpoint detection via oxidation of a methyl orange indicator solution.[2] A stock solution was prepared by dissolving

0.050 g of methyl orange and 0.25 g of KBr in 0.050 L of water and then mixing with 0.010 L of ethylene glycol. A stock solution was prepared by diluting 1:3 (v/v) using 0.100 L of 0.50 M H_2O_4(aq) and 1.0 mL of 3.0 wt% H_2O_2(aq). The indicator solution was prepared by diluting the stock solution to 1 L with deionized H_2O and Cl_2 was quantified using endpoint detection in 0.100 L aliquots of the indicator solution. The initial color and the bleached color are shown in Figure S6 and the transition during titration with Cl_2 gas was rapid, occuring in less than a second. During a typical electrolysis experiment at 0.100 A/cm^{-2}, the endpoint was reached in ~20 seconds such that the faradaic efficiency estimate represents an average efficiency during 20 seconds of electrolysis.

Technoeconomic analysis

We performed a technoeconomic analysis and sensitivity analysis to understand how various operating parameters for the chlor-iron process influence the economics of decarbonized Fe production. The levelized cost of Fe was computed for a 20-year project with a discount rate, $r = 8\%$, and an inflation rate, $i = 3.8\%$, based on the average US inflation from 1960 to 2021. The capital cost of the plant was estimated on a MT_{Cl2} day^{-1} basis, using published costs for a new membrane chlor-alkali plant (2000, converted to 2020 dollars). Capital was based on the total plant cost, so we did not include installation costs or balance of plant costs. The cost of replacing the stacks was assumed to be 20% of the total plant cost, occurring on a fixed maintenance schedule, and an annual cost of 5% of the total plant cost was included to account for maintenance. The capacity factor for both Fe and Cl_2 was assumed to be 95% and we did not calculate revenue including the sale of NaOH, assuming instead that it would be used to replenish electrolyte or be used for CO_2 capture and mineralization. The base case for the sensitivity analysis assumed an electricity price of \$75/MWh, an iron ore price of \$120/MT, a cell voltage of 3.2 V, a Cl_2 capacity factor of 95%, and a stack replacement schedule of 7 years. The levelized cost of Fe was

calculated for a given model scenario such that the net present value of the plant was equal to zero (Equation S1)

$$NPV = \sum_{y=0}^{n} \frac{R_y - O_y - S_y}{(1+r+i)^y} - CAP \qquad (S1)$$

where R_y is the yearly revenue through hydrogen sales, O_y is the yearly operating costs due to electricity consumption, and S_y is the yearly system costs due to maintenance and stack replacements. The capital expense, CAP, was the system. Cash flow in years after the first year was adjusted by r and i. Annual revenue was calculated from the product of the production capacity, P_j (MT_j day^{-1}), the capacity factor, C_j, and the levelized cost of Fe or Cl_2, where LCO_{Cl2} was held fixed at \$150/MT (Equation S2).

$$R_y = 365 \frac{\text{day}}{\text{y}} \sum_j (LCO_j) P_j C_j \qquad (S2)$$

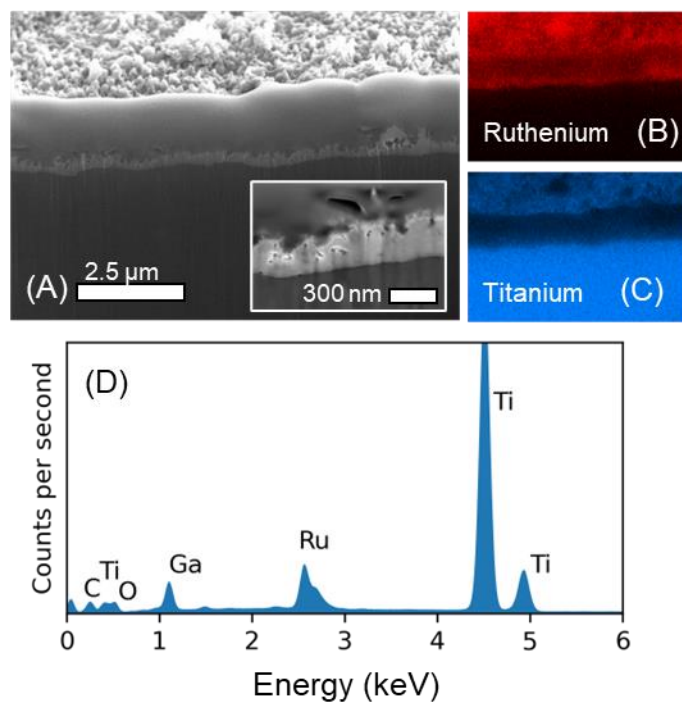**Supplementary Results and Figures**

Figure S1: (**A**) SEM image of a cross section of the Ti-supported RuOx catalyst layer used in the chlor-iron cells prepared in this report. The cross section was prepared by milling with a Ga focused ion beam.
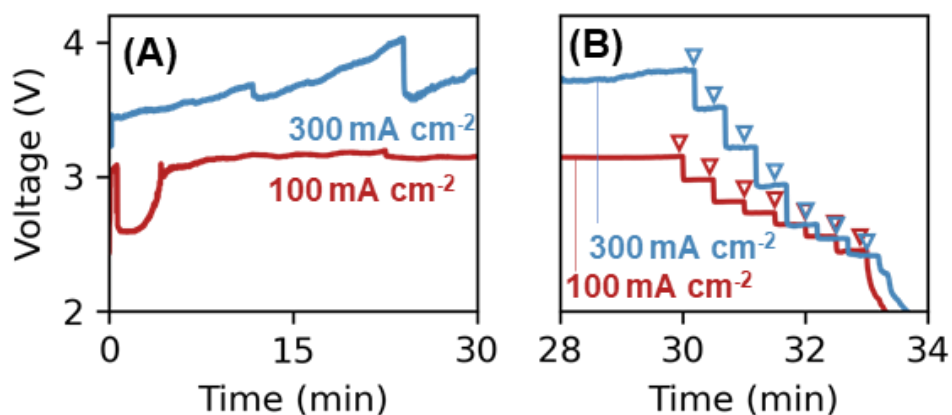

Figure S2: (**A**) Raw data collected during electrolysis at 100 mA cm^{-2} and 300 mA cm^{-2} in a batch cell. (**B**) Stepdown from operating current showing the collection of steady state voltages used to prepare a polarization curve for the cell.
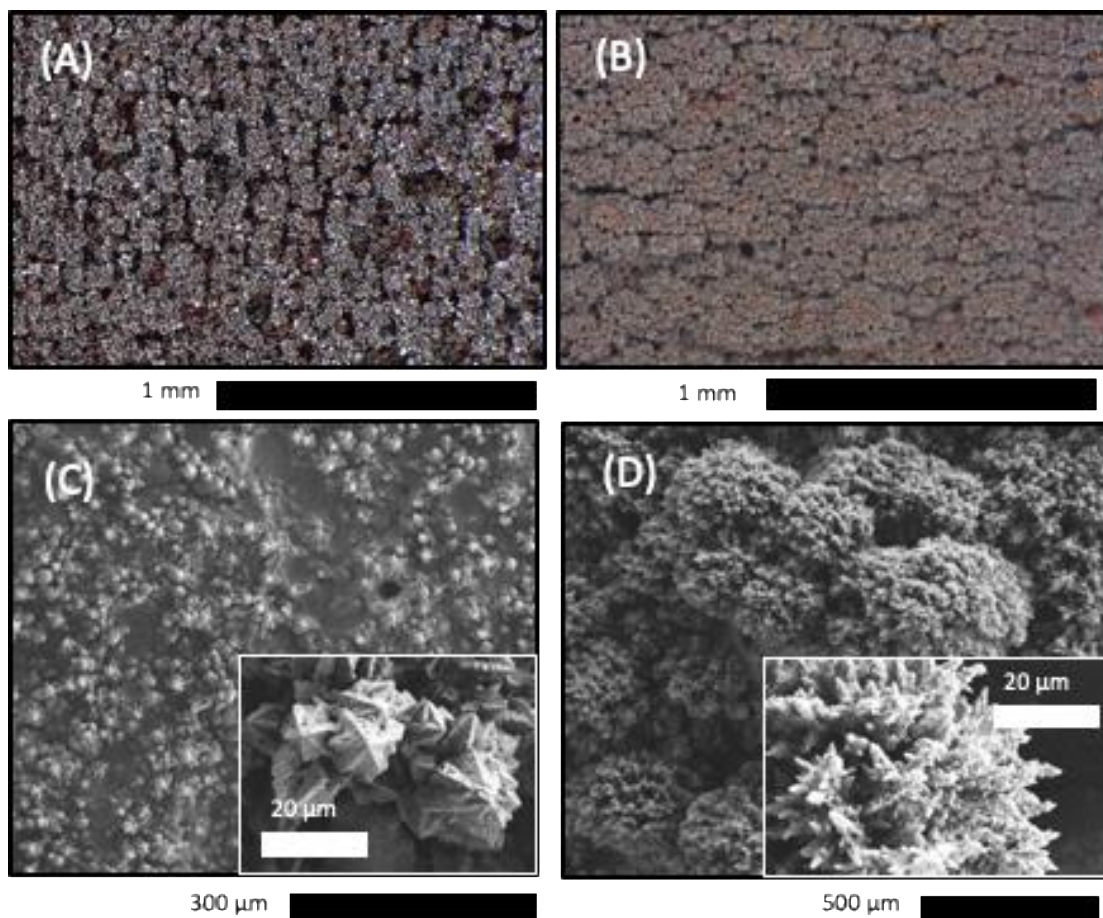
Figure S3: Top-down images of the surface morphology of Fe films as a function of the applied J. **(A)** Optical plan view image of an Fe surface after 30 min of electrolysis at $J = 100$ mA cm^{-2} and **(B)** $J = 300$ mA cm^{-2}. **(C)** Plan view SEM image of an Fe surface after 30 min of electrolysis at $J = 100$ mA cm^{-2} and **(D)** $J = 300$ mA cm^{-2}. Inset images are collected at increased magnification of the same surface.

Optical microscopy of the film cross sections revealed distinct domains, one lustrous and gray and the other dull and red in color, suggestive of metallic Fe and residual unreacted ferric oxides/hydroxides, respectively. Inspection of the reddish film surface via scanning electron microscopy (SEM) revealed small nanoparticles/nanosheets present on the faceted, metallic surface (**Figure S4**).
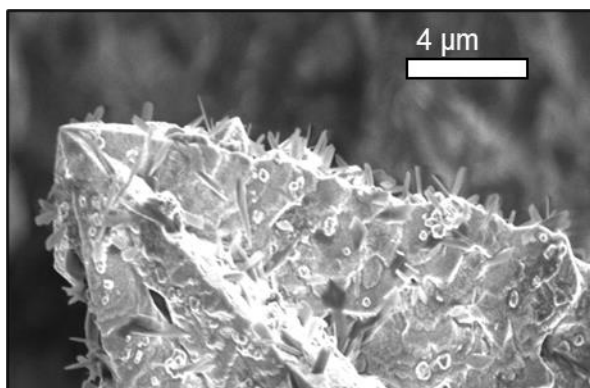
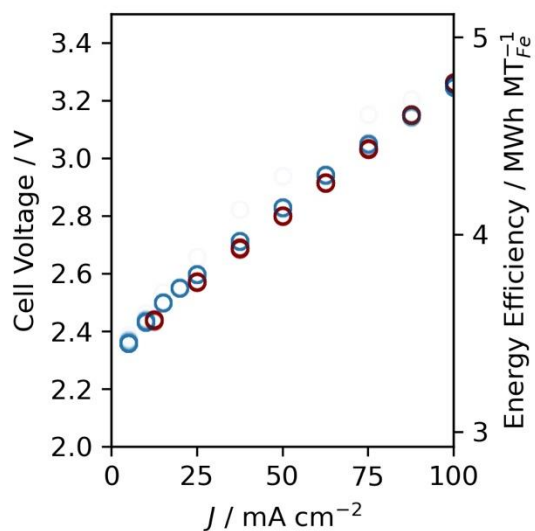**Figure S4**: Nanoparticles/nanosheets observed on Fe surface via SEM.

Figure S5: Comparison of the polarization behavior of the chlor-iron flow cell after (**A**) 30 min of electrolysis at $J = 100$ mA cm^{-2} and (**B**) 4 hours of electrolysis at $J = 100$ mA cm^{-2}. The maximum energy efficiency is computed assuming unity Faradaic efficiency towards products.
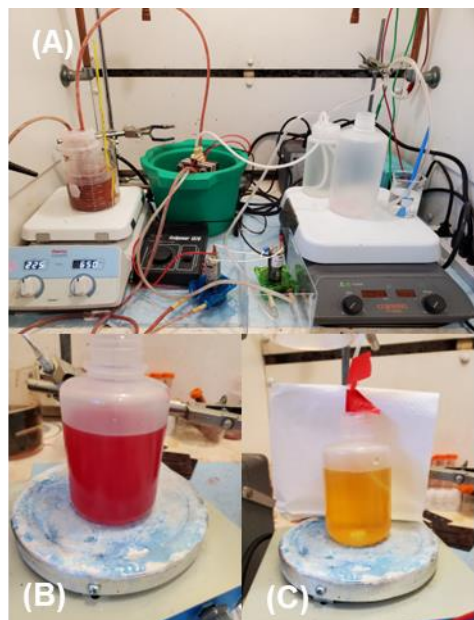
Figure S6: (A) Pre-heated catholyte and anolyte were slowly pumped into the flow cell which was maintained at a fixed temperature using external silicone heating pads. Experimental set up for Cl_2 faradaic efficiency measurements. Gaseous effluent from the anode compartment was quenched in a large beaker containing aqueous NaOH until bubbling reached a steady state. The effluent was then passed to a 1 L beaker containing a stirred methyl orange indicator solution **(B),** which rapidly bleached upon reaching a fixed endpoint **(C)**. The time required to reach the endpoint was used to calculate a molar flux of chlorine which was compared to the applied *J* to calculate a Faradaic efficiency for the cell.
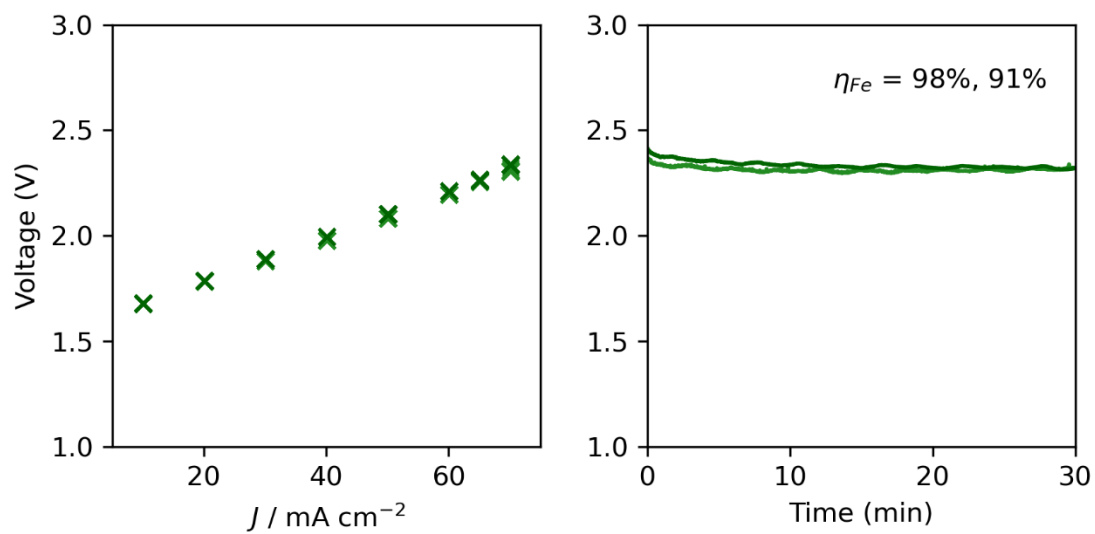
Figure S7: Current-voltage performance of a chlor-iron cell separated by a porous diaphragm (UTP500). (**A**) Polarization response of the cell after 30 min electrolysis at $J = 75$ mA cm^{-2}. (**B**) Voltage performance and η_{Fe} of a chlor-iron cell (two separate trials) separated by a porous diaphragm at a constant $J = 75$ mA cm^{-2}.
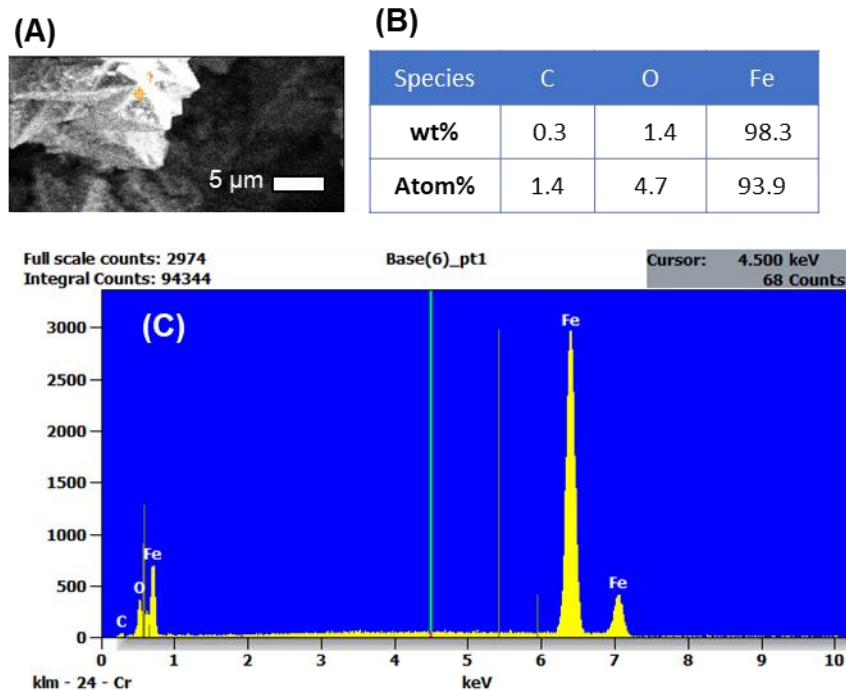
Figure S8: Elemental analysis of iron particles produced via electrolysis in the chlor-iron cell. **(A)** Particle analyzed via energy dispersive X-ray spectroscopy (EDX). **(B)** Composition of the particle in **(A)** on a weight basis and atomic percent basis. **(C)** Raw EDX spectrum used to calculate the elemental composition in **(B)**

Table S1: Reported composition of "commercial-grade" iron oxide powder

Fe	**55 %**
Fe_2O_3	82 %
MgO	1.1 %
Mn	0.4 %
Al_2O_3	2.9 %
SiO_2	8.0 %
Pb	30 ppm
As	20 ppm
Average Particle Size	500 mesh (30 μm)

Table S2: Measured η_{Fe} as a function of intentionally added SiO_2 and Al_2O_3 impurities to reactant Fe_2O_3. Each condition was measured with one replicate, with η_{Fe} measured after 30 min of continuous electrolysis.

η_{Fe} vs metal oxide concentration at 100 mA cm^{-2}

SiO_2 wt%	Al_2O_3 wt%	η_{Fe} (%)
0	0	94, 95
0	4	95, 95
8	0	58, 57
8	4	57, 54

η_{Fe} vs metal oxide concentration at 300 mA cm^{-2}

SiO_2 wt%	Al_2O_3 wt%	η_{Fe} (%)
0	0	87, 87
0	4	88, 93
8	0	36, 37
8	4	39, 41

Supplementary Discussion

Collection of iron in electrowinning cells

Electrowinning, the process of reducing metal oxide and metal sulfide ores to bulk metal, is an established industrial process. For stacks of cells that are electrically connected in parallel as opposed to series, metal can be harvested from a current collector while the remaining cells in the stack remain in operation. This maximizes the capacity factor for the cells and exerts a negligible influence on the average stack current, provided there are a significant fraction of cells left in operation. In our experiments, free-standing films of Fe were readily removed from Cu current collectors, supporting the viability of this approach. Stacks operated on intermittent renewable energy would have regular opportunities to harvest Fe from a greater number of cells at once. We are aware of at least one commercialized electrowinning process that collects Cl_2 gas generated from an acidic chloride bath used to produce Ni from ore, suggesting that simultaneous collection of solid and gaseous products can be achieved at scale.

Envisioned process for decarbonized steel production

Fe produced in chlor-iron cells could have an immediate impact on existing supply chains for Fe, namely by serving as a feedstock of primary Fe for electric arc furnaces (EAF) used to process scrap steel. To maintain sufficiently low levels of impurity in the molten product, some quantity of high purity Fe is typically added to the furnace. The purity and grain size of the Fe sponge produced in the chlor-iron cells in this report is consistent with the Fe sponge produced in the "direct reduction of iron" (DRI) process used to source primary Fe for electric arc furnaces and the markets are similar in scale in certain geographic regions of the world (e.g. Gulf Coast of the United States of America). Although the maximal impact on emissions will occur when electrified Fe can serve as a direct replacement for Fe produced in Blast Furnaces, we believe leveraging the existing DRI/EAF pathway to support a more immediate impact on emissions from steelmaking.

Capacity for abated emissions

About 8% of annual global emissions are associated with steelmaking. The capacity of the chlor-iron process to directly address these emissions depends on the amount of GHG emissions that can be avoided through steel recycling, the source of primary Fe that is replaced by the chlor-iron process, as well as the amount of offtake available for co-product Cl_2. Based on the existing Cl_2 market (~100 MMT y^{-1}) the chlor-iron process could produce up to 53 MMT_{Fe} y^{-1}, which would offset ~115 MMT_{CO2e} y^{-1} if used to replace blast furnaces and ~53 MMT_{CO2e} y^{-1} if used to replace natural-gas-based direct reduction of iron.[3] A byproduct of this production would be up to 115 MMT y^{-1} of NaOH, depending on the quantity consumed within the electrolyzers; this alkali could either be used to directly capture and mineralize 126 MMT y^{-1} of CO_2, potentially leading to a net-negative process for ironmaking. Alternatively, this NaOH(aq) could be fed to conventional Fe ore/O_2 electrolyzers,[4] which would operate at a greater levelized cost of Fe, but increased energy efficiency, and are not limited by offtake of the anodic product. This strategy could mitigate challenges associated with electrolyte fouling/consumption in alkaline cells by providing inexpensive NaOH onsite (zero transportation costs). In this manner, the unique benefit of net NaOH production can be leveraged to support multiple technology pathways to electrified ironmaking.

Supplementary References

(1) Trasatti, S.; Buzzanca, G. Ruthenium dioxide: A new interesting electrode material. Solid state structure and electrochemical behaviour. *J. Electroanal. Chem. Interfacial Electrochem.* **1971**, *29* (2), A1-A5.
(2) Wintrich, D.; Öhl, D.; Barwe, S.; Ganassin, A.; Möller, S.; Tarnev, T.; Botz, A.; Ruff, A.; Clausmeyer, J.; Masa, J. Enhancing the selectivity between oxygen and chlorine towards chlorine during the anodic chlorine evolution reaction on a dimensionally stable anode. *ChemElectroChem* **2019**, *6* (12), 3108-3112.
(3) Raabe, D.; Tasan, C. C.; Olivetti, E. A. Strategies for improving the sustainability of structural metals. *Nature* **2019**, *575* (7781), 64-74. Fan, Z.; Friedmann, S. J. Low-carbon production of iron and steel: Technology options, economic assessment, and policy. *Joule* **2021**, *5* (4), 829-862.
(4) Leduc, J. A. M.; Loftfield, R. E.; Vaaler, L. E. Electrolytic Iron Powder from a Caustic Soda Solution. *J. Electrochem. Soc.* **1959**, *106* (8), 659. DOI: 10.1149/1.2427467 (acccessed 2022-04-20T07:31:15). Haarberg, G. M.; Yuan, B. Direct electrochemical reduction of hematite pellets in alkaline solutions. *ECS Trans.* **2014**, *58* (20), 19. Allanore, A.; Lavelaine, H.; Valentin, G.; Birat, J. P.; Lapicque, F. Electrodeposition of Metal Iron from Dissolved Species in Alkaline Media. *J. Electrochem. Soc.* **2007**, *154* (12), E187. DOI: 10.1149/1.2790285 (acccessed 2022-04-27T06:23:31).